

Pretrained hybrid transformer for generalizable cardiac substructures segmentation from contrast and non-contrast CTs in lung and breast cancers

Aneesh Rangnekar¹ PhD, Nikhil Mankuzhy² MD, Jonas Willmann¹ MD, Chloe Choi¹ MS, Abraham Wu² MD, Maria Thor¹ PhD, Andreas Rimner³ MD, and Harini Veeraraghavan¹ PhD

¹Department of Medical Physics, Memorial Sloan Kettering Cancer Center, New York, NY ²Department of Radiation Oncology, Memorial Sloan Kettering Cancer Center, New York, NY

³Department of Radiation Oncology, Medical Center – University of Freiburg, Faculty of Medicine, University of Freiburg, German Cancer Consortium (DKTK), partner site DKTK-Freiburg, Freiburg, Germany

Abstract:

Introduction: AI automated segmentations for radiation treatment planning (RTP) can deteriorate when applied in clinical cases with different characteristics than training dataset. Hence, we refined a pretrained transformer into a hybrid transformer convolutional network (HTN) to segment cardiac substructures lung and breast cancer patients acquired with varying imaging contrasts and patient scan positions.

Methods: Cohort I, consisting of 56 contrast-enhanced (CECT) and 124 non-contrast CT (NCCT) scans from patients with non-small cell lung cancers acquired in supine position, was used to create oracle with all 180 training cases and balanced (CECT: 32, NCCT: 32 training) HTN models. Models were evaluated on a held-out validation set of 60 cohort I patients and 66 patients with breast cancer from cohort II acquired in supine (n=45) and prone (n=21) positions. Accuracy was measured using Dice similarity coefficient (DSC), Hausdorff distance (HD95), and dose metrics. Publicly available TotalSegmentator served as the benchmark.

Results: The oracle and balanced models were similarly accurate (DSC Cohort I: 0.80 ± 0.10 versus 0.81 ± 0.10 ; Cohort II: 0.77 ± 0.13 versus 0.80 ± 0.12), outperforming TotalSegmentator. The balanced model, using half the training cases as oracle, produced similar dose metrics as manual delineations for all cardiac substructures. This model was robust to CT contrast in 6 out of 8 substructures and patient scan position variations in 5 out of 8 substructures and showed low correlations of accuracy to patient size and age.

Conclusions: A hybrid pretrained transformer convolution network demonstrated robustly accurate (geometric and dose metrics) cardiac substructures segmentation from CTs with varying imaging and patient characteristics, one key requirement for clinical use. Moreover, the model combining pretraining with balanced distribution of NCCT and CECT scans was able to provide reliably accurate segmentations under varied conditions with far fewer labeled datasets compared to an oracle model.

Acknowledgement: This research was partially supported by the NCI R01 CA258821 and the Memorial Sloan Kettering Cancer Center Support Grant/Core Grant NCI P30 CA008748.

Introduction

Spillover radiation to cardiac substructures from radiation treatment (RT) is associated with the development of acute and late cardiac toxicities and subsequent shorter survival in patients with lung [1-3], esophageal, and breast cancers [4]. However, current radiation treatment planning (RTP) objectives often include the entire heart as a single organ, which is insufficient to differentiate the sensitivities of the individual cardiac substructures [5]. Time-consuming manual delineation of individual cardiac substructures and a lack of sufficiently accurate automated segmentation, limit the widespread use of cardiac structure-specific dose constraints.

Advances in deep learning (DL) have resulted in the development of multiple approaches to generate automated segmentation of cardiac substructures from computed tomography (CT) and magnetic resonance images (MRI). Off-the-shelf methods such as the nnU-Net [6] and other convolutional networks have demonstrated reasonable accuracies in specific disease sites, such as segmenting tumors in lung cancer patients [7] and organs at risk in breast cancer patients [8]. Commercial thoracic organ segmentation solutions based on U-Net have shown to be less accurate than in-house developed models for non-contrast CT (NCCT) scans [9]. AI models work best on testing datasets with similar characteristics as training and deteriorate when datasets with different intensity and disease characteristics are used. On the other hand, AI models used for routine clinical use must provide robustly accurate results under varying imaging and patient characteristics before they can be safely implemented in routine clinical workflows.

The goal of this work was to develop a robustly accurate DL-based cardiac substructures segmentation and evaluate its robustness to different common patient characteristics (disease, age, sex, weight) as well as imaging acquisitions (contrast-enhanced versus non-contrast, prone versus supine positions) encountered in RTP involving two different thoracic cancers.

DL models also require large numbers of manually delineated datasets for training. TotalSegmentator [10], created using the nnU-Net architecture [6], was trained on 1,204 carefully delineated scans. Transformers, a more accurate architecture than convolutional nets due to their use of multi-head self-attention to extract local and global anatomical context, also require large numbers of labeled training datasets [11]. Manual delineation of multiple cardiac substructures is labor-intensive, subject to inter-rater variations, and are challenging to perform in areas of low-soft tissue contrast, especially on NCCT scans. Methods that can generate accurate segmentations with relatively few manually labeled examples would be practical and even necessary when applied to routine clinical workflows, so that the models can be easily adapted to institutional clinical delineation guidelines and changes to imaging acquisition protocols.

Pretrained transformers overcome the need for numerous labeled task-specific datasets by learning to extract reusable features robust to imaging variations from large numbers of diverse unlabeled image datasets unrelated to the task [12]. Hence, we used a hybrid network combining a pretrained hierarchical shifted window transformer to form the encoder with a convolutional U-Net decoder

to generate cardiac substructure segmentation. The transformer was pretrained using a published method called self-distilled masked image transformer (SMIT) and with more than 10,000 CT volumes, including a variety of diseases in the thorax [13,14]. Finally, to enhance the robustness of the model when training with few labeled datasets, we used a balanced training approach, whereby the number of contrast-enhanced CT (CECT) and NCCT scans were matched. The balanced model used substantially fewer examples (N=64) compared to the oracle model (N=180). To our best knowledge, this represents the first study to employ a hybrid pretrained transformer for automated segmentation of cardiac substructures trained in data-limited regimes.

Methods and Materials

Patient cohorts

Two retrospectively collected institutional patient cohorts were analyzed following approval of the local Institutional Review Board (IRB). Cohort I, used for network training and validation, consisted of 240 CT scans from patients diagnosed with locally advanced non-small cell lung cancer (LA-NSCLC) who subsequently underwent conventionally fractionated radiation treatment [15]. Cohort II, used as a held-out test set, consisted of 66 patients diagnosed with stage I-III breast cancer who underwent radiation treatment [16].

Imaging characteristics

Cohort I consisted of a mix of 80 CECT and 160 NCCT scans of varying image quality and resolutions across different scanners. Image acquisition used a kilovoltage peak (kVp) range of 120–140, with an average voxel spacing was 1 mm x 1 mm x 3 mm. All patients were scanned in the supine position. Cohort II consisted of only NCCT scans, with patients scanned in either supine (N=45) or prone (N=21) positions.

The great vessels consisting of aorta (AA), pulmonary artery (PA), superior vena cava (SVC), and inferior vena cava (IVC), along with the four heart chambers, the right atrium (RA), right ventricle (RV), left atrium (LA), and left ventricle (LV), were manually delineated for all patient scans in both datasets using predefined institutional contouring criteria. All delineations were verified and refined as necessary by an expert radiation oncologist for quality assurance.

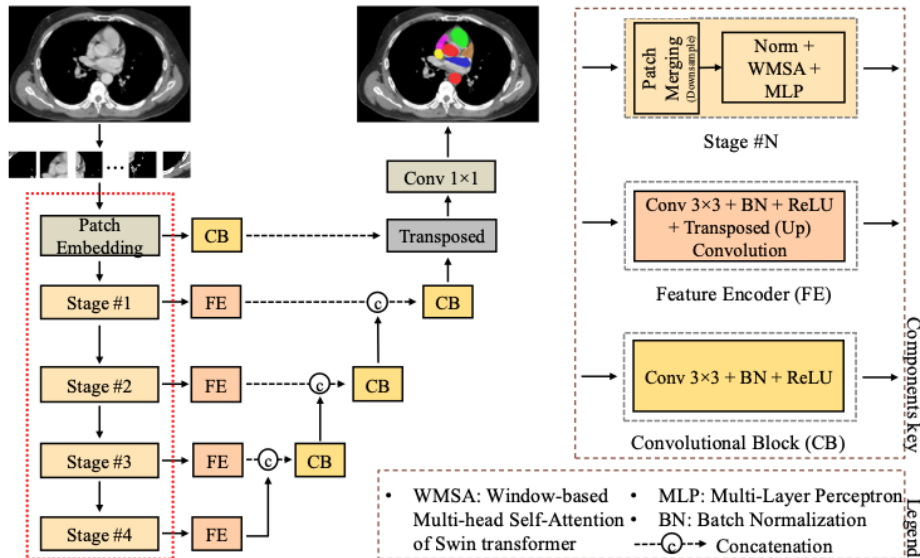


Figure 1: Architectural diagram of the pretrained hybrid transformer convolutional network, showing the transformer backbone (indicated by the dotted red box) integrated with the U-Net decoder utilized in this study.

Deep learning method

Figure 1 depicts the schematic of the hybrid transformer-convolutional network. Pretraining used the Self-distilled Masked Image Transformer (SMIT) [14], performed using 10,412 unlabeled CT volumes mostly sourced from the Cancer Imaging Archive (TCIA) with diverse diseases, including lung cancer, COVID-19, head and neck, and abdominal cancers (chest-abdomen CT). The pretraining strategy used pretext tasks such as self-distillation and masked image prediction to construct masked image portions that leveraged images themselves as the ground truth. A publicly available model checkpoint was used directly to initialize the transformer encoder, so no additional pre-training was required.

The convolutional U-Net [17] decoder was initialized from scratch and the model weights refined as part of fine-tuning with task-specific labeled data from cohort I. The U-Net decoder used skip connections that link feature maps from different stages of the transformer encoder to the decoder, ensuring that fine-grained spatial details were preserved.

Three different models were created to assess the impact of training data size as well as the relative importance of CECT versus NCCTs for providing accurate segmentations: (a) **Oracle** used the entire training set consisting of 56 CECT and 124 NCCT scans within 3-fold cross-validation to maximize the number of training samples, (b) **Balanced** model used 32 CECT and 32 NCCT scans to assess performance with fewer training samples but with balanced prevalence of different imaging contrasts, and (c) **Contrast-only** model, which used all available 56 CECT scans for training to assess model performance when trained with CECT scans that are relatively easier to manually delineate by experts due to better visualization of various cardiac substructures.

Testing was performed on a held-out testing set of 60 CTs from cohort I (24 CECT and 36 NCCT) as well as the 66 NCCTs from cohort II, never used in training the models. All models were ‘locked’ before testing.

All models were trained using a combination of soft Dice and categorical cross-entropy loss, optimized with Adam (learning rate of $2e-4$) and a cosine decay scheduler, with a batch size of 16 for 1000 epochs, and simultaneously generated segmentation of multiple cardiac substructures. The scans were normalized between [-200 HU to 300 HU] and sampled at 128 x 128 x 128 voxels with a spatial resolution of 1 mm x 1 mm x 3 mm. Standard data augmentations, including random image interpolation, cropping, and X-Y-Z rotations, were applied using the MONAI [18] and PyTorch [19] libraries. Inference was performed on the full-resolution scans using a 3D sliding window strategy with a 50% overlap. Hence, no preprocessing, including re-orientation or region cropping of images, was required for testing.

For baseline comparison, we employed the publicly available TotalSegmentator [10] model that is based on the nnU-Net [6] architecture using the published pre-trained weights, without any modifications to its internal architecture. TotalSegmentator variant *heartchambers_highres* for

segmenting the AA, PA, and the heart chambers and standard variant of TotalSegmentator for all remaining substructures were used to achieve best performance [20]. TotalSegmentator also employs test-time augmentations to provide an ensemble segmentation. We found the TotalSegmentator to be very sensitive to image orientation. Hence, all test images were reoriented on a case-by-case basis to match the anatomical alignment expected by the model and achieve the best possible segmentation.

Evaluation metrics and statistical analysis

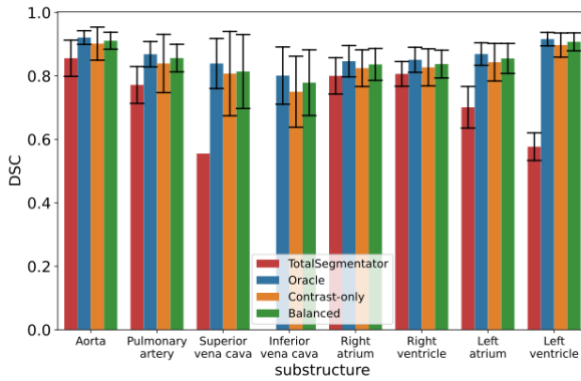
Segmentation accuracy was evaluated using the Dice similarity coefficient (DSC) and the Hausdorff distance at the 95th percentile (HD95). Statistical differences between the methods were analyzed using a two-sided, paired Wilcoxon signed rank test with 95% confidence level, and Bonferroni correction applied to adjust for multiple comparisons.

The influence of various factors on the network segmentation quality, including age and size measured using body mass index (BMI), as a continuous variable, and biological sex, image acquisition (contrast-enhanced versus non-contrast), and patient positioning (supine versus prone), were evaluated. Spearman rank correlation coefficients were computed for each cardiac substructure with respect to age and BMI. Differences in segmentation accuracy for categorical variables (image acquisition, patient position, and biological sex) were assessed using two-sided, unpaired Wilcoxon signed-rank tests with a 95% significance level.

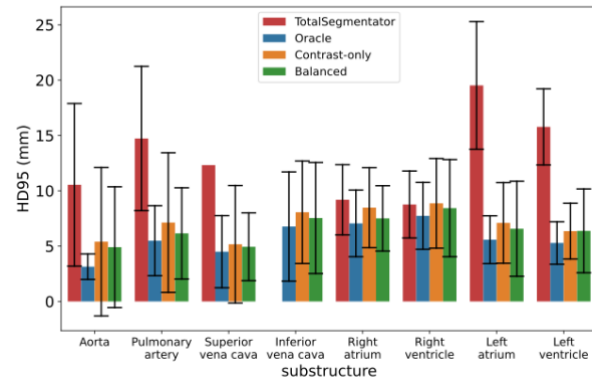
Dose metrics including maximum dose (DMax) and mean dose (DMean) were calculated for all cardiac substructures from the dose maps using the manual delineations as well as the AI generated segmentations. PA was evaluated separately using V40Gy [21].

Results

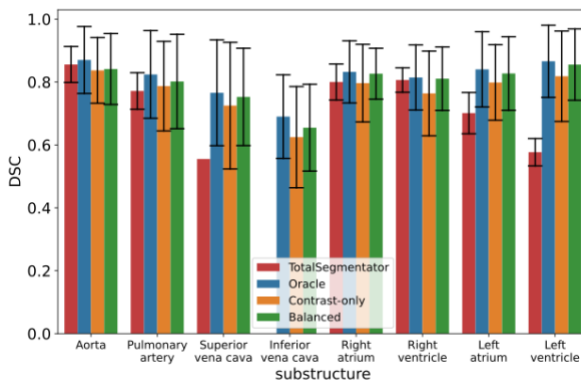
Balanced model using fewer training examples resulted in similarly accurate segmentations as the Oracle model



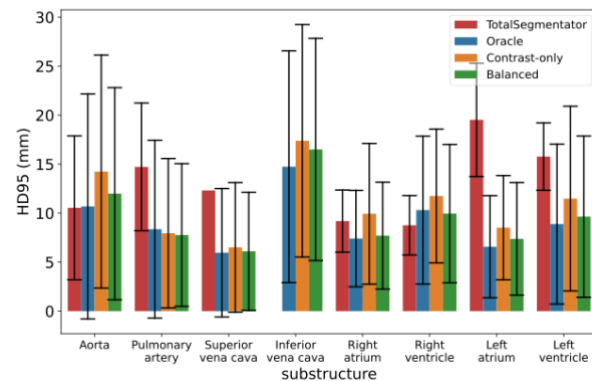
(a)



(b)



(c)



(d)

Figure 2: Segmentation performance in analyzed test cohorts using Dice Similarity Coefficient (DSC) and 95th percentile Hausdorff Distance (HD95) metrics. Panels a and b correspond to cohort I, while c and d represent cohort II. Error bars represent the standard deviation across test cases.

The balanced model was similarly accurate for the analyzed cardiac substructures in both cohorts I and II (Figure 2, Supplemental Tables S1 and S2). Statistical comparisons showed no differences in accuracies for the various cardiac substructures (Supplemental Tables S3 and S4). In comparison, the contrast-only model using 54 CECT scans resulted in worse accuracies compared to the oracle in cohort I, particularly for IVC ($p = 0.0196$), RV ($p = 0.023$), and LV ($p = 0.006$).

This same model produced significantly inaccurate segmentations for multiple structures except SVC and RA compared to the oracle in cohort II using only NCCT cases.

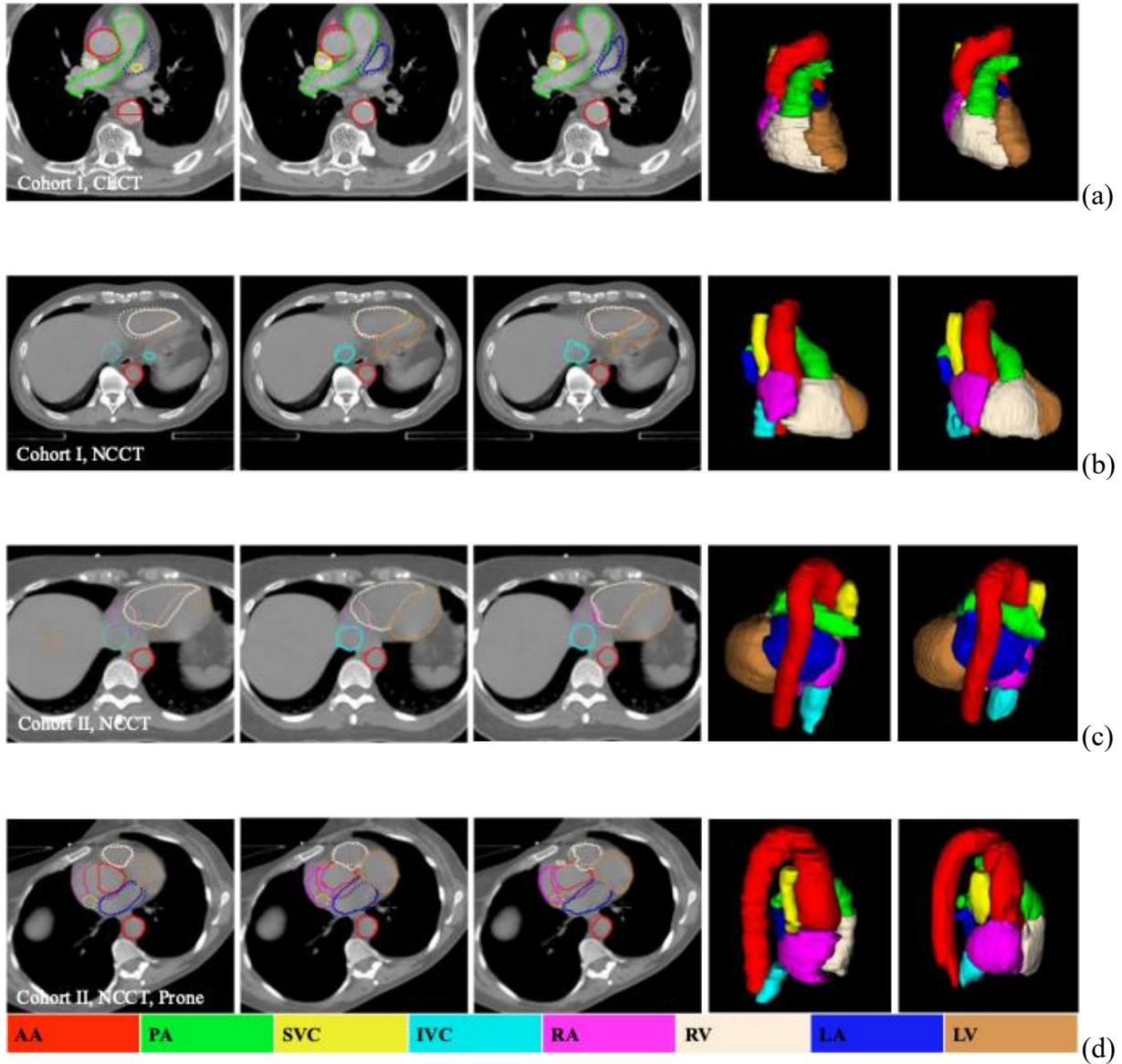


Figure 3: Representative scans (a–d) from cohorts I and II, showing CECT and NCCT acquisitions. Auto-segmentations from TotalSegmentator, Oracle, and Balanced models (solid lines) are displayed together with manual delineations (dotted lines). Final two columns show 3D renderings for the balanced model auto-segmentations and manual delineations respectively.

TotalSegmentator model produced worse accuracies compared to balanced and oracle models in both cohort I and cohort II. It segmented only 6 out of the 8 cardiac structures in both cohorts. IVC was not segmented, and SVC was segmented only in one patient for cohort I (indicated by lack of error bar) and none in cohort II. Representative example cases from cohort I and II on CECT and NCCT cases scanned under prone and supine positions with segmentations generated by balanced, oracle, and TotalSegmentator models are shown in Figure 3. As shown, balanced and oracle models closely followed clinical delineations compared to the TotalSegmentator. These results indicate that the balanced model, despite training with only 64 cases, compared to 180 used in the oracle model and 1,204 by TotalSegmentator, was sufficiently accurate in both patient cohorts involving two different cancers.

Balanced model produced segmentations robust to analyzed patient and imaging characteristics

The balanced as well as other models were further evaluated to assess robustness to variations in patient characteristics (age, BMI, biological sex) and imaging acquisitions (contrast, orientation). As shown in Figure 4, balanced model showed a low correlation to the patient age, indicated by the highest Spearman rank correlation coefficient, ρ of 0.2 for AA and IVC. Patient BMI resulted in a moderate correlation of ρ of 0.4 for PA and low correlation for all the other organs. The oracle also showed a similar correlation with the analyzed cardiac substructures as balanced model (Supplemental Figures S1, S2, and S3). TotalSegmentator, which segmented only 6 out of the 8 cardiac substructures, showed a higher moderate correlation of 0.5 for PA with respect to patient age and similar correlation as balanced and oracle models with respect to BMI. Contrast-only model was less impacted by patient variations due to age but showed higher correlations for multiple cardiac substructures due to size. None of the models were impacted by patient anatomy differences due to biological sex. However, TotalSegmentator in general produced much lower accuracies than all other models for the analyzed patient characteristics (Supplemental Figure S4).

The balanced model produced similar accuracies for various cardiac substructures from NCCT and CECT scans, with differences observed for two structures including the SVC ($p = 0.0063$) and RA ($p = 0.013$). The oracle model also showed a lower accuracy for SVC ($p = 0.03$), indicating segmentation of vessels with and without contrast impacts accuracy irrespective of training data size. TotalSegmentator showed significantly lower accuracy for 4 out of 8 cardiac structures for NCCT versus CECT, indicating poor robustness to contrast variations despite being trained on the largest number of training examples of the four analyzed models (Supplemental Figure S5). The contrast-only model also resulted in significantly worse accuracies for 5 out of 8 cardiac substructures on NCCT images.

The impact of image acquisition position was not evaluated for TotalSegmentator as it is very sensitive to position and required preprocessing and manual correction of images to the expected position on a case-by-case basis. Similarly, as the contrast-only model showed inaccurate

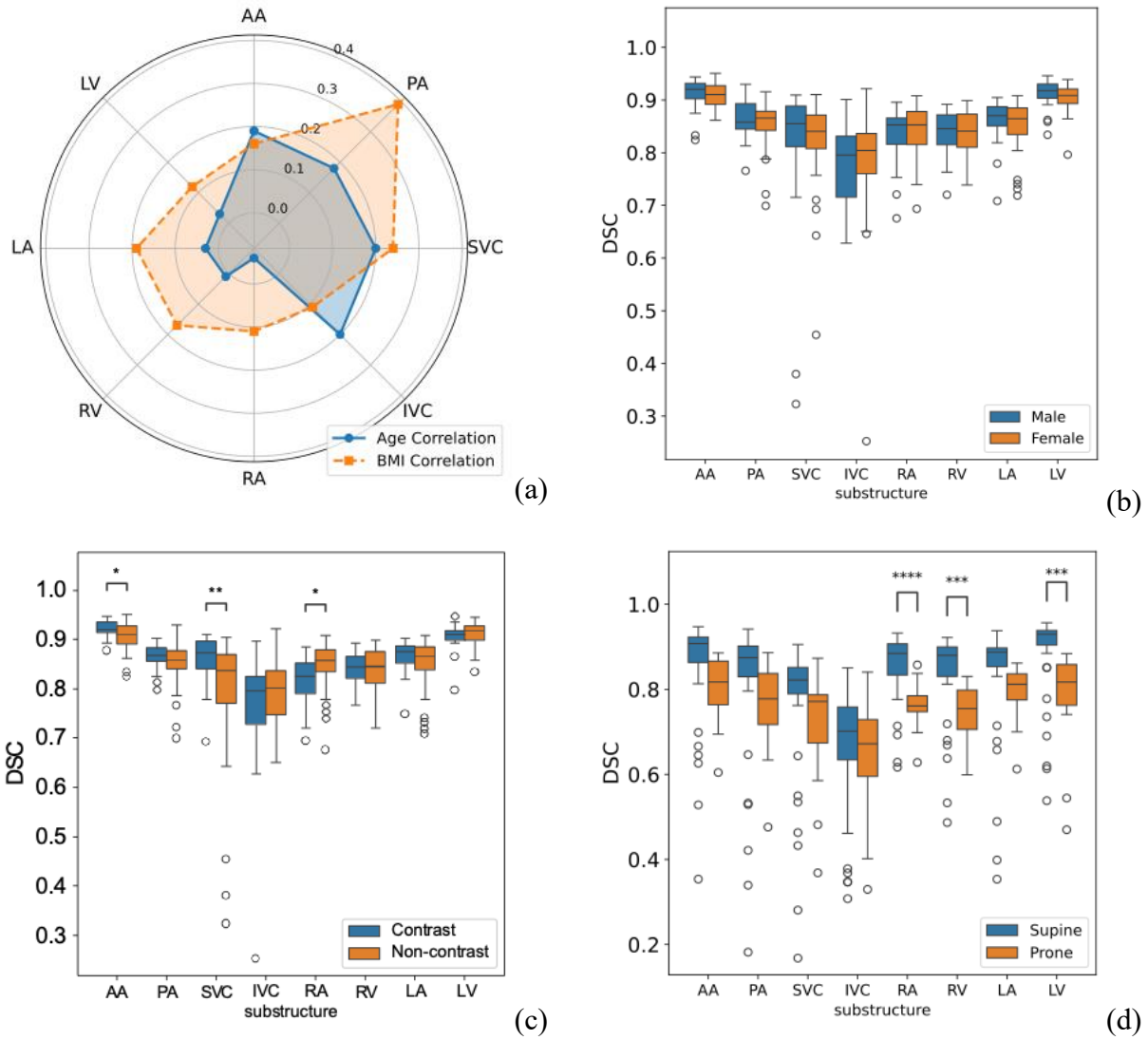


Figure 4: Segmentation performance of the Balanced model for analyzed variations in (a) age and BMI, (b) biological sex, (c) presence of intravenous contrast, and (d) scan orientation. Analyses in (a–c) used cohort I; (d) used cohort II. * indicates level of statistical significance (*: $p < 0.05$, **: $p < 0.01$, ***: $p < 0.001$, ****: $p < 0.0001$).

performance for NCCT cases, this analysis was not pursued as patients with varied image positions were all scanned with NCCT. The balanced model was robust to differences in patient imaging position for 5 cardiac substructures and showed decreased accuracy in prone position for heart chambers including RA ($p = 0.0005$), RV ($p = 0.0003$), and LV ($p = 0.0006$). In comparison, the oracle model also produced lower accuracy for the same three cardiac substructures RA ($p = 0.042$), RV ($p = 9.25e-06$), and LV ($p = 3.81e-04$), indicating that the models were impacted due to a domain shift from training exclusively on patients scanned in supine position (Supplemental Figure S6).

Balanced model produced similar dose metrics as manual delineations

Table 1 presents the dosimetric comparison between manual delineation and the balanced model segmentations for various cardiac substructures. As shown, the dose metrics were statistically similar. Scatter plot showing dose metrics extracted using the balanced model and manual segmentations show strong correlation for all analyzed cardiac substructures (Supplemental Figure S7). Figure 5 shows three cases with the largest dose deviations occurring between balanced model

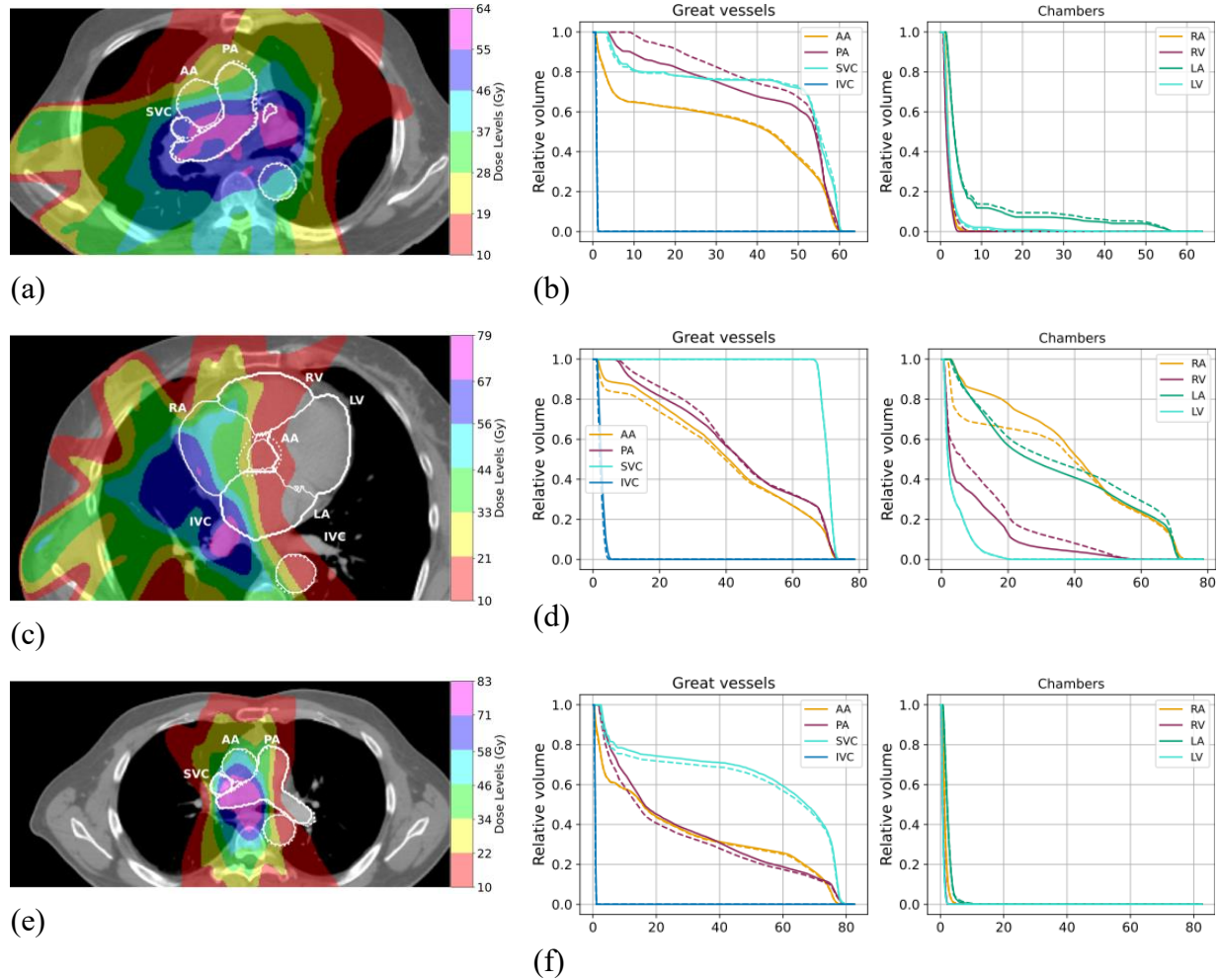


Figure 5: Comparison of radiation dose distributions (a, c, e) and corresponding dose–volume histograms (DVHs) (b, d, f) for the balanced model on three representative scans from cohort I. Solid lines indicate balanced model generated segmentations; dotted lines indicate manual delineations.

segmentations (dotted lines) and the manual delineations (solid lines), visualized as dose-volume histogram (DVH) curves. Specifically, in the first case, the AI segmentations resulted in higher DVH metrics for aorta. In the second case, the AI model resulted in lower DVH values for RA and higher values for RV, indicating under- and over-segmentation for these structures, respectively.

In the third case, the AI model segmentations resulted in similar DVH metrics for all analyzed structures as the manual delineations. These results indicate that the balanced model could provide reasonably similar dose metrics as manual delineations.

	Metric (Gy)	Manual delineation	Balanced model	p-value
Aorta	DMax	67.63 ± 6.784	67.66 ± 6.765	0.97
Pulmonary artery	V40	66.13 ± 21.45	65.48 ± 21.07	0.82
Superior vena cava	DMax	64.21 ± 11.45	64.30 ± 11.55	0.96
Inferior vena cava	DMax	8.853 ± 15.31	8.056 ± 14.32	0.75
Right atrium	DMean	15.12 ± 14.14	15.30 ± 14.66	0.99
Right ventricle	DMean	7.941 ± 7.455	7.902 ± 7.295	0.96
Left atrium	DMean	27.56 ± 14.42	26.63 ± 14.09	0.68
Left ventricle	DMean	7.396 ± 7.257	7.159 ± 7.092	0.85
Table 1: Dosimetric comparison between manual delineations and balanced model generated segmentations. Mean and standard deviation values are reported. V40 denotes the percentage of volume receiving at least 40 Gy.				

Discussion

This study introduced a hybrid pretrained transformer encoder with a convolutional decoder approach to segment multiple cardiac substructures from NCCT and CECT scans in patients with lung and breast cancers. Our analysis showed that a pretrained model that balanced the distribution of NCCT and CECT scans provided consistently accurate segmentations across multiple analyzed patient characteristics, including contrast, scan position, age, sex, and disease sites, with far fewer examples than an oracle model. In comparison, open-source TotalSegmentator [10,20], created using the nnU-Net [6] model and trained on 1,204 labeled examples, was inconsistently accurate across the evaluated conditions. Our results show that pretrained transformer models can enhance the segmentation performance, which is consistent with previous work reporting their robustness to imaging variability for segmenting tumors [12]. Ours, on the other hand, for the first time, evaluated pretrained models' performance to various patient as well as imaging characteristics, and in the context of changing the distribution of training data. We showed that robust performance can be achieved with relatively simple approaches like balancing the prevalence of CECT and NCCT scans during data preparation as well as leveraging open source pretrained foundational models, which can be implemented in different institutional settings. Furthermore, the capability to refine models with relatively few labeled examples would also ensure safe clinical implementation and easy adaptation to any changes in imaging acquisition and delineation guidelines.

Multiple prior works used standard convolutional networks [10,15,22-25] and showed reasonably accurate segmentations for multiple cardiac substructures from MRI and CT scans, respectively. Our work focused on improving the robustness of the AI models under common clinical conditions, including applicability to breast cancer patients acquired in prone and supine positions, following training with only lung cancer patients scanned in the supine positions.

Another important factor impacting the practical implementation of AI models is the number of preprocessing steps involved in generating the segmentations. For instance, the 2D DeepLab model [15] required lung segmentation using a separate model before generating cardiac substructure segmentation. Similar approaches were used by Finnegan [24] and Oevert [25] to first extract the heart before extracting the cardiac substructures. In addition to the number of steps and training involved for those steps, the accuracy of such serial staged models could be impacted by inaccuracies in the earlier stages, thus reducing accuracy overall. Clinical implementation of multi-stage models would also require additional validation and testing at individual stages. Our model, on the other hand, can directly process volumetric CT scans without requiring any preprocessing. It is also robust to imaging orientation differences, unlike was observed for TotalSegmentator [10], which required a case-by-case review and manual correction of orientation to achieve the best possible result, which is not practical in clinical workflows.

Our study had a few limitations. First, the analysis was restricted to a single institution dataset owing to the practical limitations of performing multi-institutional evaluation due to patient privacy concerns. Second, the current study did not undertake an evaluation of potential reduction in contouring time by clinicians as the goal was to develop and assess robustness of models to varied patient and imaging characteristics.

Conclusion

We developed and evaluated a hybrid pretrained transformer encoder-convolutional decoder network to segment cardiac substructures from CT scans under common imaging variations and patient characteristics. Our results showed that combining pretrained hybrid transformers with balanced distribution of CECT and NCCT scans in training was able to produce robustly accurate performance on two distinct patient cohorts with different disease and imaging acquisitions, despite using a relatively small number of labeled datasets compared to an oracle model. Further studies will focus on evaluation of model robustness in multi-institutional cohorts.

References

- [1] Friedes C, Iocolano M, Lee SH, et al. The effective radiation dose to immune cells predicts lymphopenia and inferior cancer control in locally advanced NSCLC. *Radiother Oncol.* 2024;190:110030. doi:10.1016/j.radonc.2023.110030.
- [2] Xu C, Jin JY, Zhang M, Liu A, Kong FS, Lin SH, et al. The impact of the effective dose to immune cells on lymphopenia and survival of esophageal cancer after chemoradiotherapy. *Radiother Oncol.* 2020;146:180-186. doi:10.1016/j.radonc.2020.02.015.
- [3] Yu Y, Fu P, Jin JY, Gao S, Wang W, Machtay M, et al. Impact of effective dose to immune cells (EDIC) on lymphocyte nadir and survival in limited-stage SCLC. *Radiother Oncol.* 2021;162:26-33. doi:10.1016/j.radonc.2021.06.020.
- [4] Stoltzfus KC, Zhang Y, Sturgeon K, Sinoway LI, Trifiletti DM, Chinchilli VM, Zaorsky NG. Fatal heart disease among cancer patients. *Nature Communications.* 2020. doi: 10.1038/s41467-020-15639-5.
- [5] Bowen Jones S, Marchant T, Saunderson C, McWilliam A, Banfill K. Moving beyond mean heart dose: The importance of cardiac substructures in radiation therapy toxicity. *J Med Imaging Radiat Oncol.* 2024;68(8):974-986. doi: 10.1111/1754-9485.13737.
- [6] Isensee F, Jaeger PF, Kohl SA, Petersen J, Maier-Hein KH. nnU-Net: a self-configuring method for deep learning-based biomedical image segmentation. *Nature Methods.* 2021;18(2):203-211. doi: 10.1038/s41592-020-01008-z.
- [7] Carles M, Kuhn D, Fechter T, et al. Development and evaluation of two open-source nnU-Net models for automatic segmentation of lung tumors on PET and CT images with and without respiratory motion compensation. *Eur Radiol.* 2024;34(10):6701-6711. doi: 10.1007/s00330-024-10751-2.
- [8] Saha M, Jung JW, Lee SW, Lee C, Lee C, Mille MM. A deep learning segmentation method to assess dose to organs at risk during breast radiotherapy. *Phys Imaging Radiat Oncol.* 2023. doi: 10.1016/j.phro.2023.100520.
- [9] Chen X, Mumme RP, Corrigan KL, Mukai-Sasaki Y, Koutroumpakis E, Palaskas NL, et al. Deep learning-based automatic segmentation of cardiac substructures for lung cancers. *Radiother Oncol.* 2024. doi: 10.1016/j.radonc.2023.110061.
- [10] Wasserthal J, Breit HC, Meyer MT, Pradella M, Hinck D, Sauter AW, et al. TotalSegmentator: robust segmentation of 104 anatomic structures in CT images. *Radiology Artif Intell.* 2023. doi: 10.1148/ryai.230024.
- [11] Ma D, Hosseinzadeh Taher MR, Pang J, et al. Benchmarking and boosting transformers for medical image classification. *Proceedings of the MICCAI Workshop on Domain Adaptation and*

Representation Transfer. Cham: Springer Nature Switzerland; 2022. doi: 10.1007/978-3-031-16852-9_2.

[12] Jiang J, Rangnekar A, Veeraraghavan H. Self-supervised learning improves robustness of deep learning lung tumor segmentation models to CT imaging differences. *Med Phys*. Published online December 5, 2024. doi:10.1002/mp.17541.

[13] Liu Z, Lin Y, Cao Y, Hu H, Wei Y, Zhang Z, et al. Swin transformer: Hierarchical vision transformer using shifted windows. *Proceedings of the IEEE/CVF International Conference on Computer Vision*. 2021:10012–10022. doi:10.48550/arXiv.2103.14030.

[14] Jiang J, Tyagi N, Tringale K, Crane C, Veeraraghavan H. Self-supervised 3D anatomy segmentation using self-distilled masked image transformer (SMIT). *Medical Image Computing and Computer-Assisted Intervention – MICCAI 2022*. Cham: Springer Nature Switzerland; 2022:556–566. doi: 10.1007/978-3-031-16440-8_53.

[15] (Redacted for double-blind anonymity)

[16] (Redacted for double-blind anonymity)

[17] Ronneberger O, Fischer P, Brox T. U-net: Convolutional networks for biomedical image segmentation. *Medical Image Computing and Computer-Assisted Intervention – MICCAI 2015*. Vol 9351. Springer; 2015:234–241. doi: 10.1007/978-3-319-24574-4_28.

[18] Cardoso MJ, Li W, Brown R, et al. MONAI: An open-source framework for deep learning in healthcare. *arXiv*. 2022. doi: 10.48550/arXiv.2211.02701.

[19] Paszke A, Gross S, Massa F, et al. PyTorch: An imperative style, high-performance deep learning library. *Advances in Neural Information Processing Systems*. 2019. doi: 10.48550/arXiv.1912.01703.

[20] Hinck D, Segeroth M, Miazza J, et al. Automatic segmentations of cardiovascular structures on chest CT datasets: An update of the TotalSegmentator. *Eur J Radiol*. 2025. doi: 10.1016/j.ejrad.2025.112006.

[21] Harris WB, Zou W, Cheng C, Jain V, Teo BKK, Dong L, et al. Higher dose volumes may be better for evaluating radiation pneumonitis in lung proton therapy patients compared with traditional photon-based dose constraints. *Adv Radiat Oncol*. 2020. doi: 10.1016/j.adro.2020.06.023.

[22] Morris ED, Ghanem AI, Dong M, Pantelic MV, Walker EM, Glide-Hurst CK. Cardiac substructure segmentation with deep learning for improved cardiac sparing. *Med Phys*. 2020. doi: 10.1002/mp.13940.

- [23] Harms J, Lei Y, Tian S, McCall NS, Higgins KA, Bradley JD, et al. Automatic delineation of cardiac substructures using a region-based fully convolutional network. *Med Phys*. 2021. doi: 10.1002/mp.14810.
- [24] Finnegan RN, Chin V, Chlap P, et al. Open-source, fully-automated hybrid cardiac substructure segmentation: Development and optimisation. *Phys Eng Sci Med*. 2023;46(1):377–393. doi: 10.1007/s13246-023-01231-w.
- [25] Van Den Oever LB, Spoor DS, Crijns APG, et al. Automatic cardiac structure contouring for small datasets with cascaded deep learning models. *J Med Syst*. 2022;46(5):22. doi: 10.1007/s10916-022-01810-6.

Supplemental

DSC accuracies for the various cardiac substructures using analyzed models for testing data from Cohort I									
	Aorta	PA	SVC	IVC	RA	RV	LA	LV	
TotalSeg mentator	0.86 ±0.06	0.77 ± 0.06	0.55 (1 scan)	-	0.80 ± 0.06	0.80 ± 0.04	0.70 ± 0.07	0.58 ± 0.04	
Oracle	0.92 ± 0.02	0.87 ± 0.04	0.85 ± 0.06	0.80 ± 0.08	0.85 ± 0.04	0.86 ± 0.04	0.87 ± 0.03	0.92 ± 0.02	
Contrast- only	0.90 ± 0.05	0.84 ± 0.09	0.81 ± 0.13	0.75 ± 0.11	0.82 ± 0.06	0.83 ± 0.06	0.84 ± 0.06	0.90 ± 0.04	
Balanced	0.91 ± 0.03	0.86 ± 0.04	0.81 ± 0.12	0.78 ± 0.10	0.84 ± 0.05	0.84 ± 0.04	0.86 ± 0.05	0.91 ± 0.03	
HD95 (mm) for the various cardiac substructures using analyzed models for testing data from Cohort I									
	Aorta	PA	SVC	IVC	RA	RV	LA	LV	
TotalSeg mentator	10.5 ± 7.35	14.7 ± 6.52	12.3 (1 scan)	-	9.19 ± 3.17	8.76 ± 3.02	19.5 ± 5.78	15.8 ± 3.44	
Oracle	3.08 ± 1.22	5.56 ± 3.39	4.14 ± 2.73	6.67 ± 4.11	6.69 ± 2.77	7.32 ± 3.23	5.80 ± 2.55	5.01 ± 1.95	
Contrast- only	5.40 ± 6.70	7.13 ± 6.31	5.17 ± 5.31	8.06 ± 4.63	8.48 ± 3.62	8.87 ± 4.05	7.10 ± 3.64	6.35 ± 2.52	
Balanced	4.91 ± 5.46	6.15 ± 4.12	4.94 ± 3.06	7.54 ± 5.02	7.51 ± 2.95	8.43 ± 4.39	6.57 ± 4.29	6.38 ± 3.79	

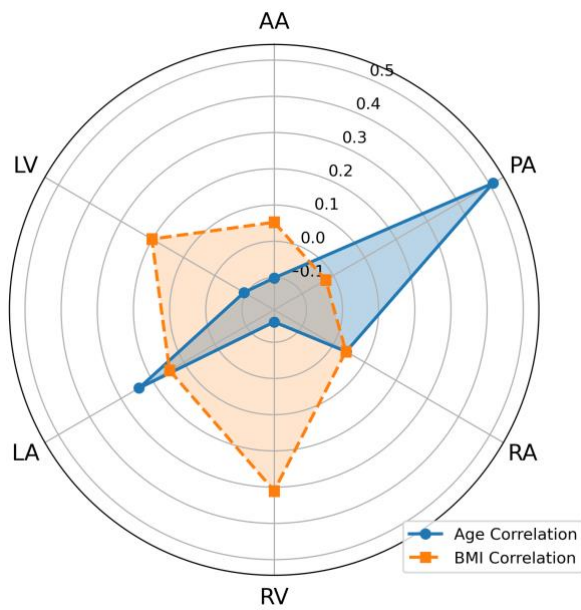
Table S1: Dice Similarity Coefficient (DSC) and 95th percentile Hausdorff Distance (HD95) for different anatomical substructures using analyzed models from Cohort I.

Cardiac substructures	Contrast-only versus Oracle				Balanced versus Oracle			
	DSC		HD95		DSC		HD95	
	p-value	p-value*	p-value	p-value*	p-value	p-value*	p-value	p-value*
Aorta	0.0424	0.0848	0.0839	0.1679	0.0258	0.0517	0.0467	0.0933
Pulmonary artery	0.0310	0.0618	0.1111	0.2222	0.0641	0.1282	0.2516	0.5032
Superior vena cava	0.1087	0.2175	0.2605	0.5211	0.1318	0.2636	0.0869	0.1739
Inferior vena cava	0.0059	0.0119	0.0209	0.0418	0.0705	0.1411	0.0859	0.1718
Right atrium	0.0097	0.0196	0.0067	0.0135	0.2177	0.4354	0.2505	0.5010
Right ventricle	0.0012	0.0231	0.1075	0.2150	0.1250	0.2500	0.4841	0.9682
Left atrium	0.0063	0.1271	0.0076	0.0152	0.1076	0.2151	0.1506	0.3031
Left ventricle	0.0033	0.0064	0.0099	0.0199	0.1237	0.2474	0.0821	0.1642

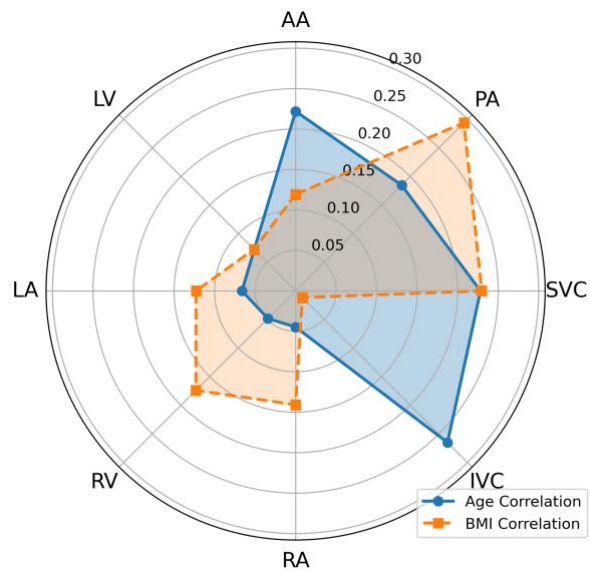
Table S3: Two-sided, paired Wilcoxon signed rank test results comparing the individual models with respect to the Oracle for various cardiac substructures from Cohort I. Asterisks (*) indicate p-values after applying Bonferroni correction.

Cardiac substructures	Contrast-only versus Oracle				Balanced versus Oracle			
	DSC		HD95		DSC		HD95	
	p-value	p-value*	p-value	p-value*	p-value	p-value*	p-value	p-value*
Aorta	0.0002	0.0004	0.0056	0.0112	0.0168	0.0336	0.0721	0.1443
Pulmonary artery	0.0128	0.0256	0.3743	0.7487	0.1432	0.2865	0.767	0.999
Superior vena cava	0.1879	0.3758	0.2848	0.5694	0.1451	0.2904	0.1918	0.3837
Inferior vena cava	0.0109	0.0219	0.1324	0.2648	0.1348	0.2697	0.0992	0.1983
Right atrium	0.0609	0.1219	0.0301	0.0602	0.3385	0.6774	0.7681	0.9999
Right ventricle	0.0048	0.0098	0.0513	0.1025	0.6570	0.999	0.9708	0.9999
Left atrium	0.0015	0.0030	0.0011	0.0022	0.1732	0.3463	0.2763	0.5526
Left ventricle	0.0004	0.0009	0.0018	0.0036	0.3751	0.7501	0.4449	0.8889

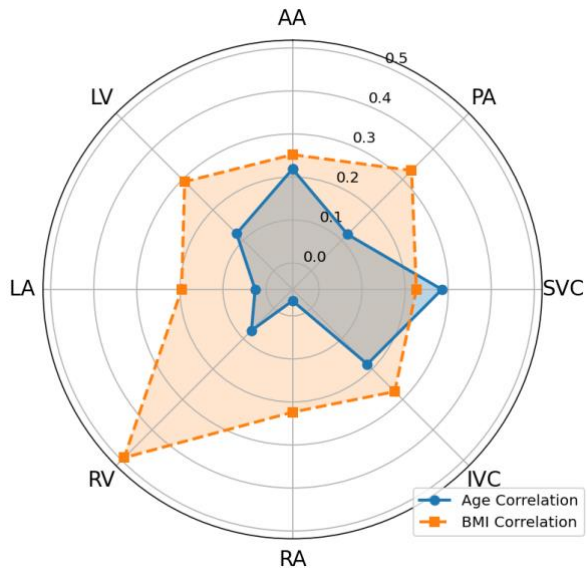
Table S4: Two-sided, paired Wilcoxon signed rank test results comparing the individual models with respect to the Oracle for various cardiac substructures from Cohort II. Asterisks (*) indicate p-values after applying Bonferroni correction.



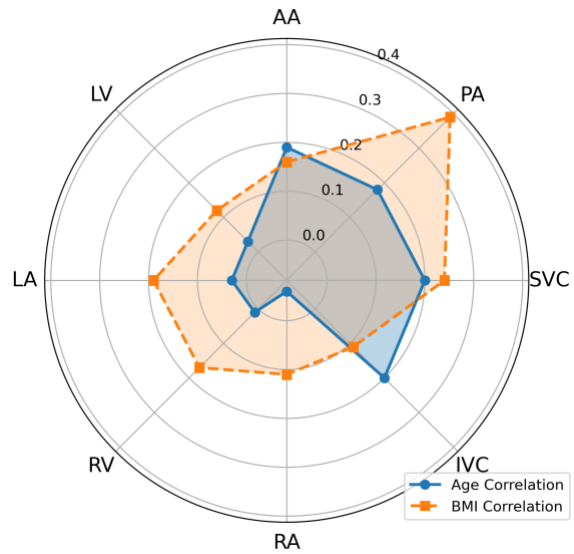
(a) TotalSegmentator



(b) Oracle

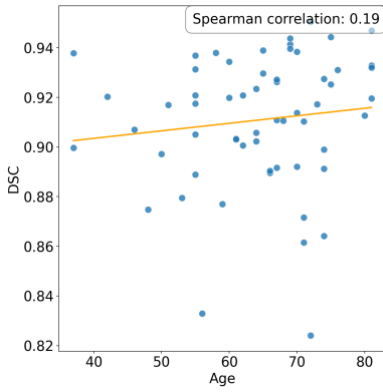


(c) Contrast-only

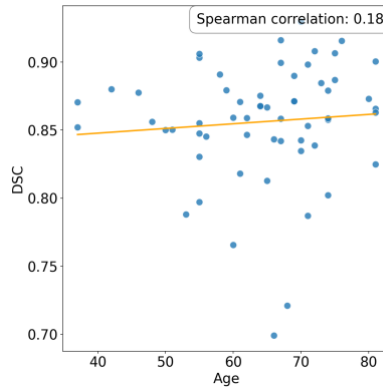


(d) Balanced

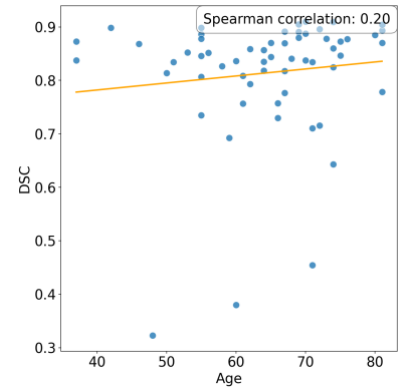
Figure S1: Spearman rank correlation coefficient of models' accuracies with respect to age and BMI from Cohort I.



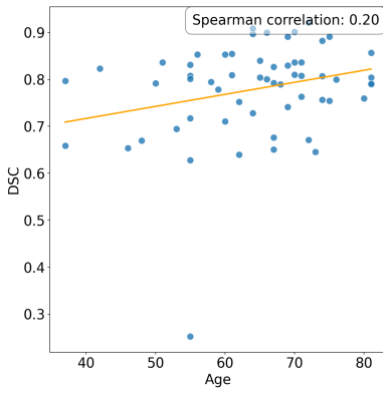
(a) Aorta



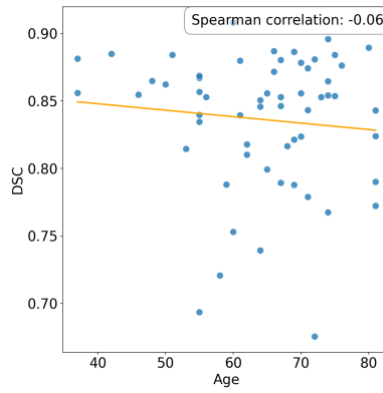
(b) Pulmonary artery



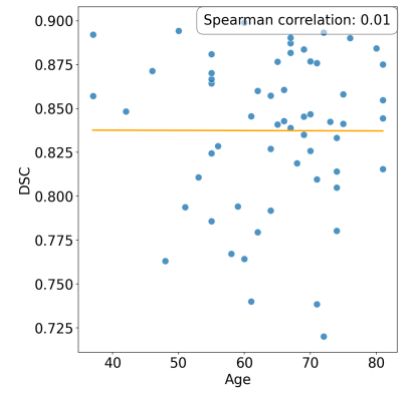
(c) Superior vena cava



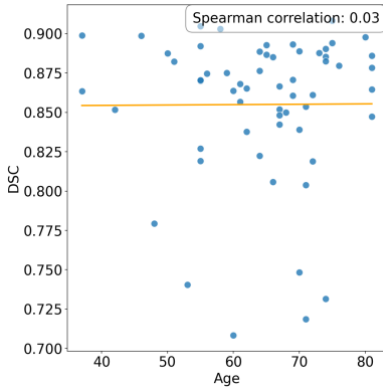
(d) Inferior vena cava



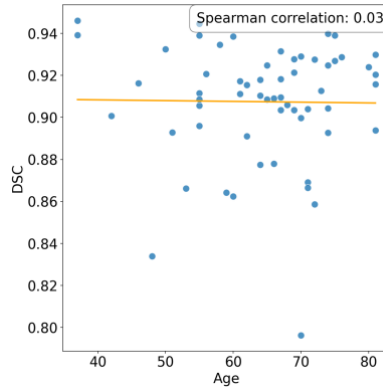
(e) Right atrium



(f) Right ventricle

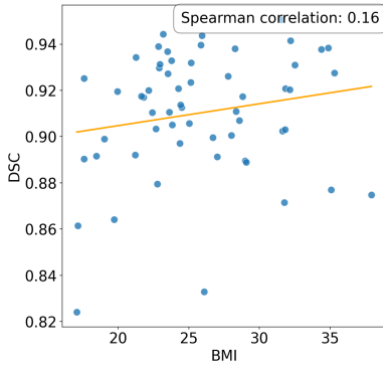


(g) Left atrium

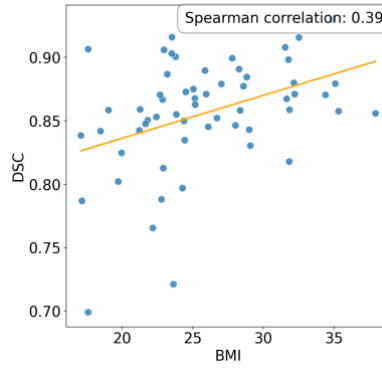


(h) Left ventricle

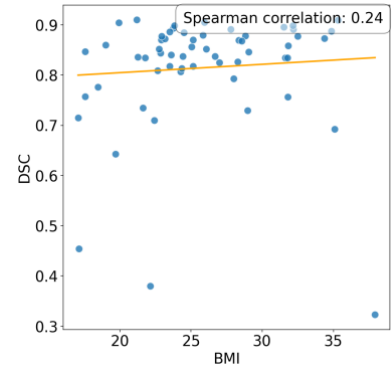
Figure S2: Scatter plots depicting the relationship between patient age and Dice Similarity Coefficient (DSC) for cardiac substructures using the balanced model on Cohort I. Spearman rank correlation coefficients are shown in the top right of each plot.



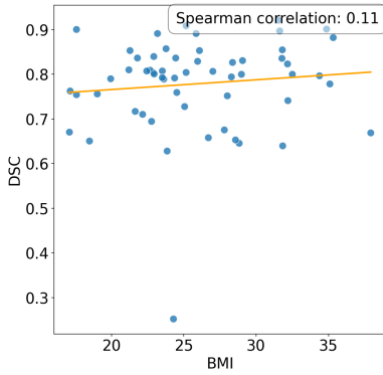
(a) Aorta



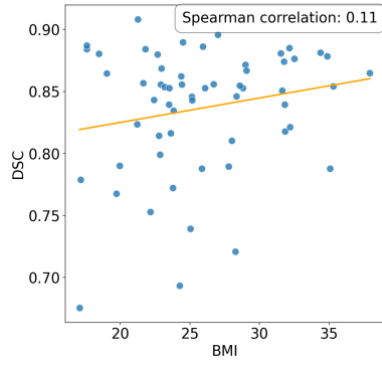
(b) Pulmonary artery



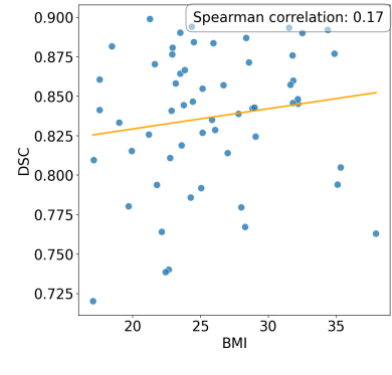
(c) Superior vena cava



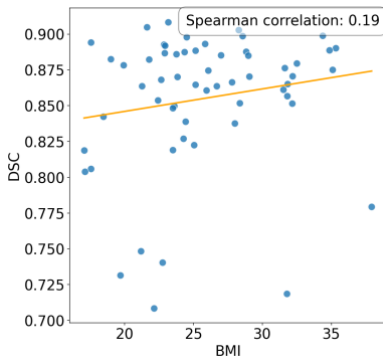
(d) Inferior vena cava



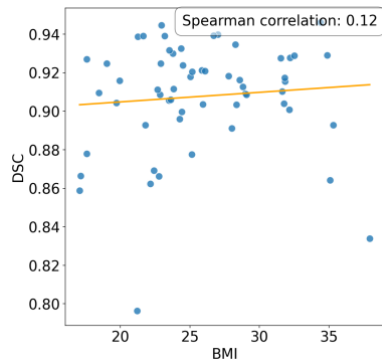
(e) Right atrium



(f) Right ventricle

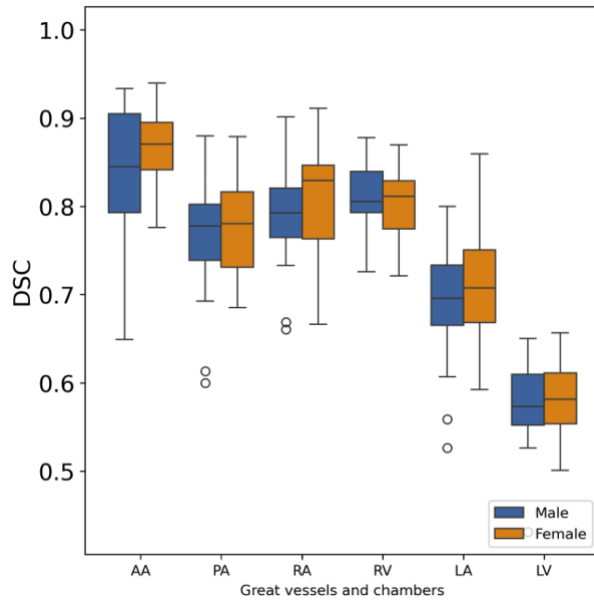


(g) Left atrium

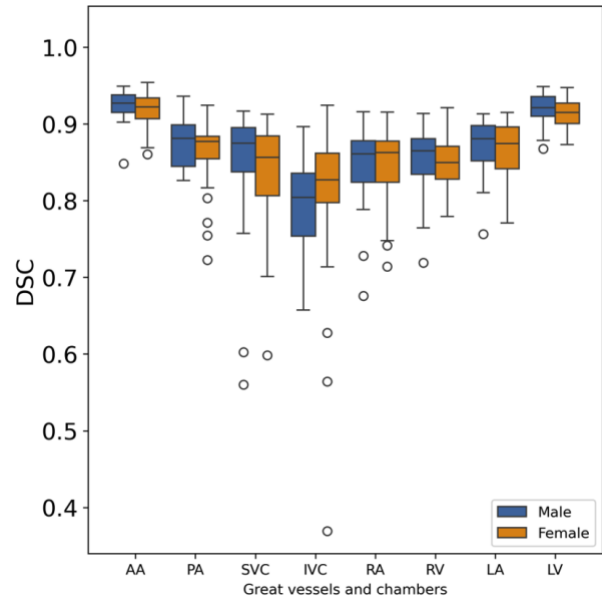


(h) Left ventricle

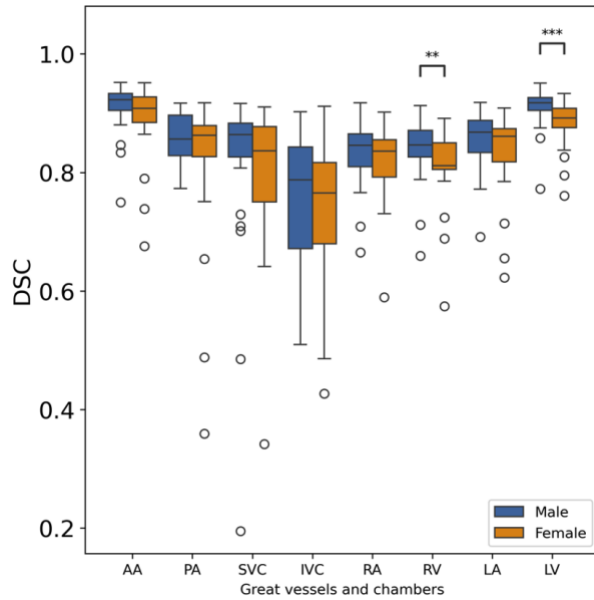
Figure S3: Scatter plots depicting the relationship between body mass index (BMI) and Dice Similarity Coefficient (DSC) for cardiac substructures using the balanced model on Cohort I. Spearman rank correlation coefficients are displayed in the top right of each plot.



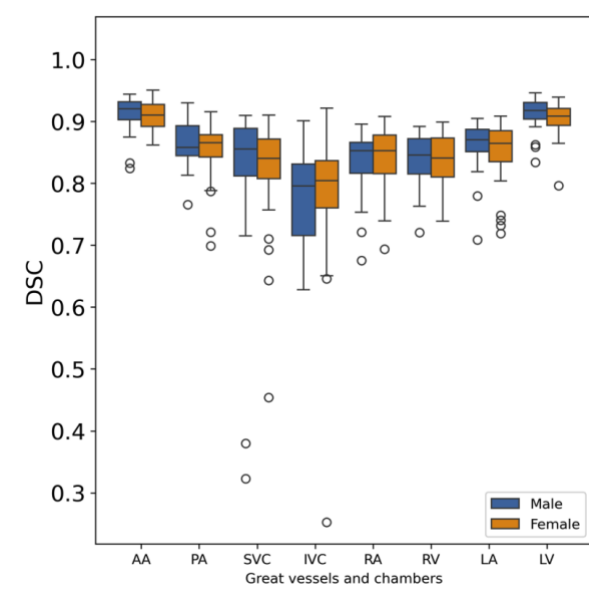
(a) TotalSegmentator



(b) Oracle

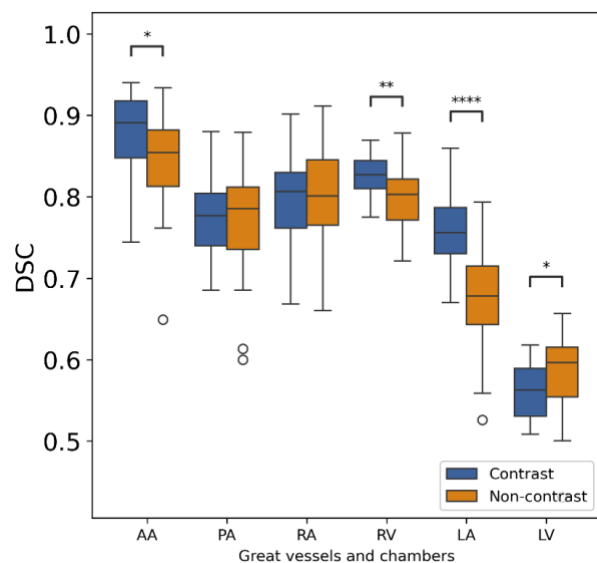


(c) Contrast-only

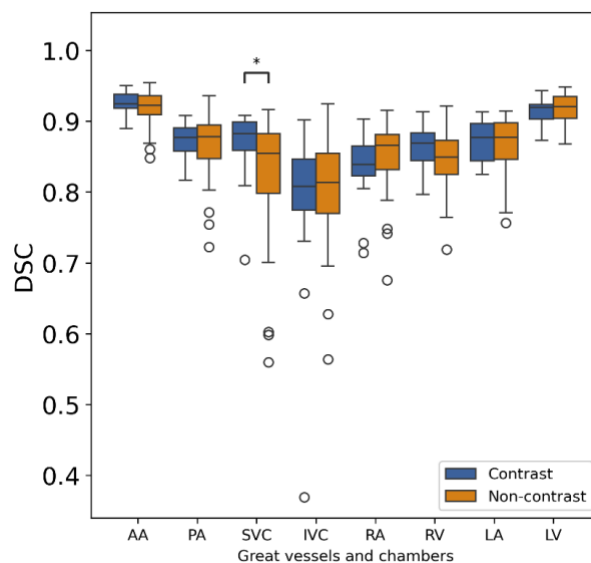


(d) Balanced

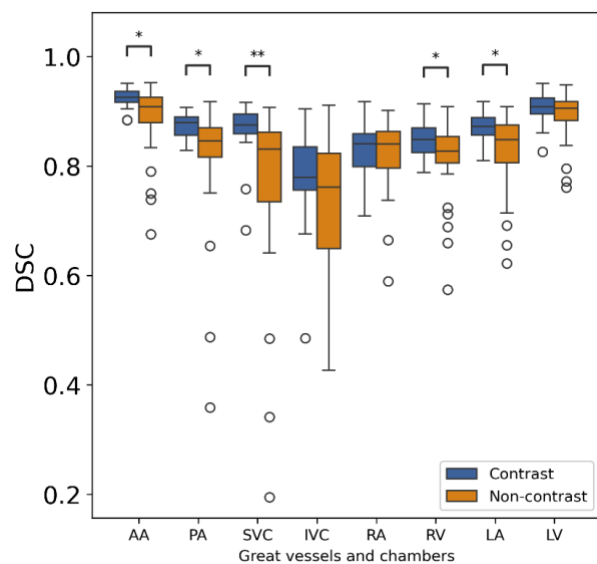
Figure S4: Segmentation performance of various models with respect to biological sex on scans from Cohort I. * indicates level of statistical significance (*: $p < 0.05$, **: $p < 0.01$, ***: $p < 0.001$).



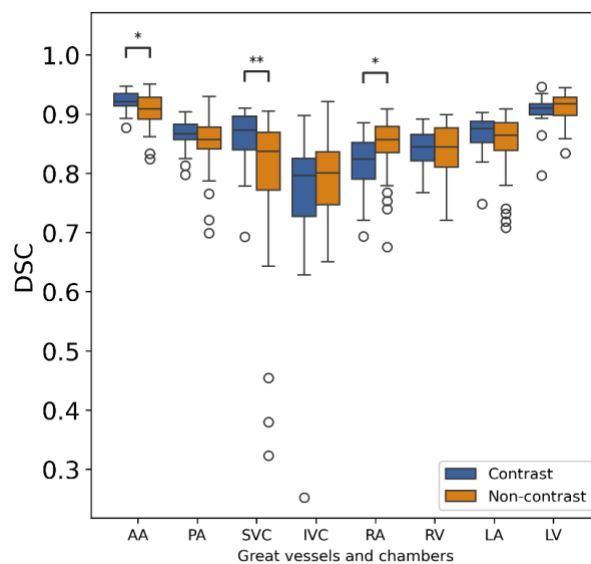
(a) TotalSegmentator



(b) Oracle

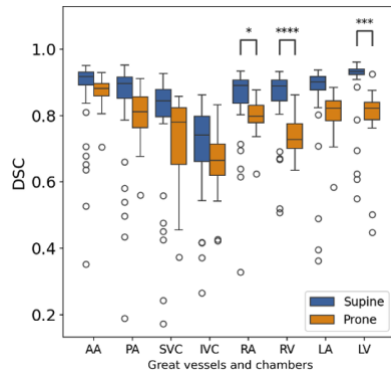


(c) Contrast-only

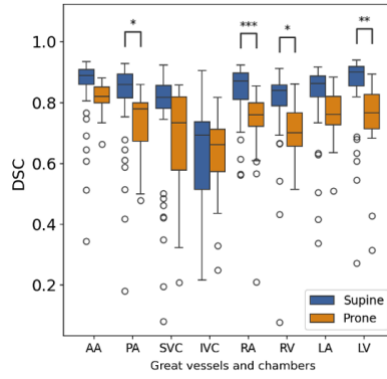


(d) Balanced

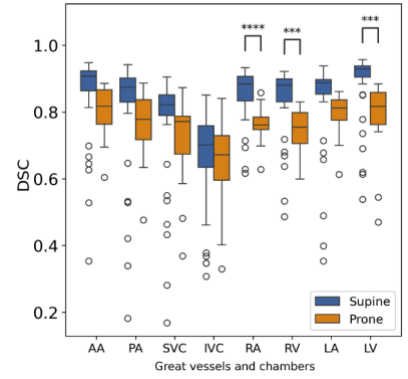
Figure S5: Segmentation performance of various models with respect to intravenous contrast differences from Cohort I. * indicates level of statistical significance (*: $p < 0.05$, **: $p < 0.01$, ***: $p < 0.001$, ****: $p < 0.0001$).



(a) Oracle

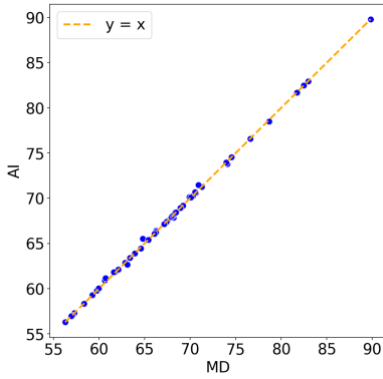


(b) Contrast-only

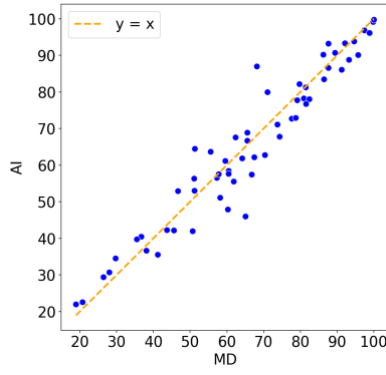


(c) Balanced

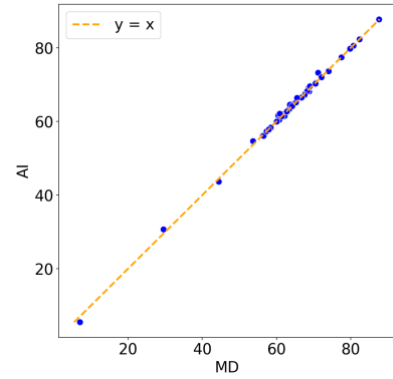
Figure S6: Segmentation performance of various models with respect to scanning position (orientation) on scans from Cohort II. * indicates level of statistical significance (*: $p < 0.05$, **: $p < 0.01$, ***: $p < 0.001$).



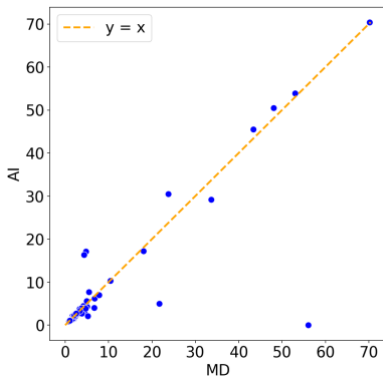
(a) Aorta



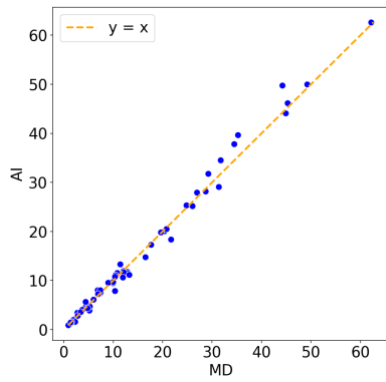
(b) Pulmonary artery



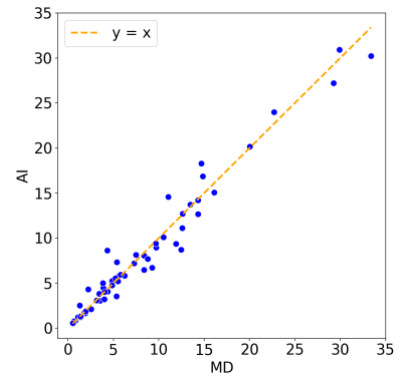
(c) Superior vena cava



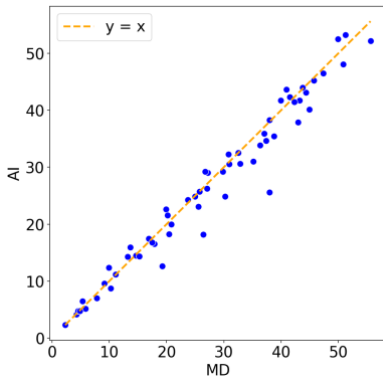
(d) Inferior vena cava



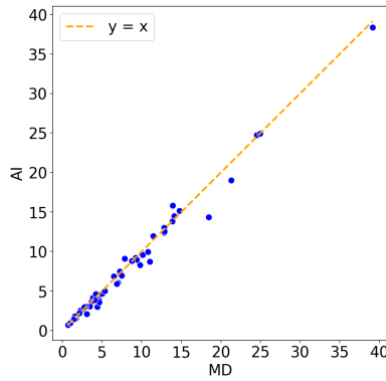
(e) Right atrium



(f) Right ventricle



(g) Left atrium



(h) Left ventricle

Figure S7: Scatter plots comparing dosimetric metrics between manual delineations (MD) and auto-segmentations (AI) from the balanced model for different cardiac substructures in Cohort I. The dashed orange line ($y = x$) indicates perfect agreement.